RSC Advances

PAPER

View Article Online
View Journal | View Issue

Cite this: *RSC Adv.*, 2026, **16**, 29423

Bandgap tuning through the substitution of alkali metal cations in A_2AlCuF_6 (A = K, Rb, and Cs) for optoelectronic and renewable energy applications

Muhammad Yaqoob,[a] Nora Mobark Farhan,[b] Hudabia Murtaza,[c] Quratul Ain,[c] Rawiyah Alkahtani,[b] Junaid Munir *[a] and M. S. Al-Buriahi[d]

Received 6th April 2026
Accepted 13th May 2026

DOI: 10.1039/d6ra02893d

rsc.li/rsc-advances

Perovskite halides are an attractive choice for renewable energy harvesting as these materials offer high flexibility and bandgap tunability. This study interrogates the first principles analysis of A_2AlCuF_6 (A = K, Rb, and Cs) done *via* DFT simulations. The FP-LAPW approach is employed to assess the physical attributes of A_2AlCuF_6 (A = K, Rb, and Cs). The structural attributes reveal a significant increase in lattice constant and ground state energy as the A-site cation is replaced by K → Rb → Cs, while the reported bulk modulus reveals a declining trend. The negative formation energies and the tolerance factor values confirm thermodynamic and structural stability. The electronic bandgap reveals an increasing trend as the A-site is replaced by K → Rb → Cs, revealing indirect bandgaps of 2.80 eV, 2.78 eV and 3.10 eV for K_2AlCuF_6, Rb_2AlCuF_6 and Cs_2AlCuF_6, respectively. The optical analysis suggests that among the studied halides, Cs_2AlCuF_6 reports high absorption and minimum energy loss in the UV region, making it an ideal candidate for UV shields and UV photodetectors. The thermoelectric attributes reveal high *ZT* values at elevated temperatures, revealing that K_2AlCuF_6, Rb_2AlCuF_6 and Cs_2AlCuF_6 are suitable contenders for the production of energy from waste heat.

Introduction

Energy is a crucial pillar of modern technologies, contributing significantly to socioeconomic growth by raising the standard of living.[1] The growing reliance on fossil fuels has resulted in a number of environmental issues, including resource depletion and climate change.[2,3] Environmental pollution and energy crises have emerged as the main obstacles to sustainable development in the context of the fast growth of global industry. In addition to having a finite supply, using traditional fossil fuels causes significant air pollution and greenhouse gas emissions.[4] Clean and sustainable energy has become a global need and has encouraged significant interest in discovering advanced materials capable of supporting the next generation of renewable energy solutions.[5–8] Among these, perovskite materials have gained prominence due to their remarkable versatility and wide-ranging applications, including solar cells, thermoelectric devices, and light-emitting technologies.[9,10] The origin of perovskite materials can be traced back to the early 1800s, when Russian mineralogist Gustav Rose recognized a naturally occurring mineral in Russia's Ural Mountains.[11] Later, perovskite halides were discovered in the early 2000s, following the discovery of organic and inorganic halide perovskites, specifically methyl ammonium lead iodide, which shows dominant efficiency in solar cell applications.[12,13] Perovskite halides generally follow the general formula ABX_3, where A-site and B-site represent cationic elements, and X-site is occupied by a halide.[14,15] A notable variant known as double perovskite halides, represented by the formula $A_2BB'X_6$, possesses great importance for its exceptional flexibility in tuning its physical properties.[16,17] Fluoride-based double perovskites, particularly those with an elpasolite-type structure, have drawn attention due to their distinctive features such as broad bandgaps, strong chemical stability, low environmental toxicity, and high dielectric constants.[18] The role of fluorine is crucial in chemical modification, hybridization in nonlinear optical crystals, UV frequency conversion and many more cases.[19–21] These properties make them highly suitable for use in renewable energy technologies such as clear solar cells and radiation sensing systems.[22] Perovskite halides possess long charge carrier diffusion lengths, strong light absorption, and cost-effective manufacturing, leading to a significant transformation in photovoltaic technology.[23,24] The *ab initio* study of $CsGeF_3$ revealed that the material remains ductile till 40 GPa pressure.[25] A first principle analysis of alkali-based halides $Rb_2ZnRuCl_6$ and $Cs_2ZnRuCl_6$ revealed that these halides are mechanically and dynamically stable with bandgap in the range of 1.53 eV to

[a]*Department of Physics, Riphah International University, Lahore, Pakistan. E-mail: junaid_ij2000@yahoo.com*
[b]*Department of Chemistry, College of Science, Princess Nourah bint Abdulrahman University, P.O. Box 84428, Riyadh 11671, Saudi Arabia*
[c]*Department of Physics, University of Management and Technology, Lahore, Pakistan*
[d]*Department of Physics, Sakarya University, Sakarya, Turkey*

1.54 eV.[26] The DFT-based analysis of Cs_3QR_6 revealed that these halides possess bandgaps from 0.54 eV to 2.79 eV, when the HSE06 potential is employed to assess the electronic traits. Furthermore, strong polarization is seen in the visible region, highlighting that these materials are excellent contenders for photovoltaic and optoelectronic applications.[27] The DFT-based analysis of K_2AgSbI_6 exhibits its strong optical interaction with an external electric field, revealing its potential for field-effect optical modulators and photo-detectors.[28] Direct bandgaps of 1.32 eV to 1.73 eV are revealed for Sr_3BiX_3 (X = I, Br, and Cl), suggesting that these materials possess strong visible-light absorption and excellent thermoelectric traits.[29] SCAPS-1D simulations revealed that Z_2MgGeI_6 (Z = Na and K) are stable and have a power conversion efficiency of 30%, highlighting their suitability for optoelectronics.[30] The thermoelectric analysis of Li_2ScAuZ_6 (Z = I, Br, and Cl) reveals notable *ZT* and power factor values, which suggest that these halides are suitable for energy-harvesting technologies.[31] An increase in lattice constant is noticed in K_2ScInX_6 as X is replaced from "F" to "I". Furthermore, direct bandgaps are noticed for all halides, revealing high absorption in the visible region.[32] The optical analysis of $(Rb/Cs)_2MgZn(Cl/Br)_6$ reports a low energy loss and strong incident light absorption in the UV range, predicting their potential for optoelectronic applications.[33] The creation of sustainable and ecologically friendly materials has become a top priority as the globe moves towards renewable energy sources. Due to their decreased toxicity, enhanced environmental compatibility, and intriguing optoelectronic and energy-related features, lead-free perovskite and double-perovskite compounds have garnered a lot of attention in this area. The novelty of investigating lead-free A_2AlCuF_6 (A = K, Rb, and Cs) using the FP-LAPW approach in this study lies in offering the first thorough and extremely accurate explanation of their inherent characteristics without the need for pseudo-potential approximations. Within a coherent theoretical framework provided *via* the Wien2K code, this study offers a methodical comparison of structural stability, electronic band structure and bonding properties that are dependent on alkali metals. These findings identify A_2AlCuF_6 (A = K, Rb, and Cs) compounds as a unique and unexplored class of lead-free fluoride double perovskites with potential applications in optoelectronics.

Computational analysis

The density functional theory-based code Wein2K is used to assess the physical attributes of A_2AlCuF_6 (A = K, Rb, and Cs). The FP-LAPW approach, which is the most accurate methodology to assess the overall physical attributes of materials with high precision, is used to analyze the physical attributes of A_2AlCuF_6 (A = K, Rb, and Cs). In this technique, the spherical harmonics is used to analyze the electrons in the muffin-tin region, whereas plane waves are used to analyze the electrons in the interstitial region.[34] The exchange–correlation effects in the crystal structures are treated with the TB-mBJ approximation,[35] which is mathematically stated as:

$$V_X^{mBJ}(r) = cV_X^{BR}(r) + (3c-2)\frac{1}{\pi}\sqrt{\frac{5}{12}}\sqrt{\frac{2t(r)}{\rho((r))}} \quad (1)$$

The above equation describes the expression for the modified mBJ approximation and "*c*" is given as:

$$c = \alpha + \beta\left(\frac{1}{V_{cell}}\int\frac{\nabla\rho(r)}{\rho(r)}\right)^{\frac{1}{2}} \quad (2)$$

The alpha and beta possess numerical values of 0.012 and 1.023 $Bohr^{1/2}$. The lowest energy and the equilibrium volume of the studied crystal structure are determined through the Birch–Murnaghan equation of state. Several crucial parameters for the convergence of force, charge and energy in the cycle are ensured by setting RMT × K_{max}, l_{max}, and G_{max} as 7, 12, and 14 $(a.u)^{-1}$, respectively. The muffin-tin regions for K/Rb/Cs, Al, Cu and F are selected as 2.48, 2.33, 2.23, and 1.89 $(a.u)^{-1}$, respectively. To avoid the overlapping spheres, the cut-off energy is selected as −8 Ryd. For the convergence of the charge and energy within the crystal structures, the convergence criteria are set to 0.0001 e $(a.u)^{-3}$ and 0.1 mRy per unit cell. A dense mesh of 3000 *k*-points is generated in the first Brillouin zone for unit cell integrations. The crystal structure for A_2AlCuF_6 (A = K, Rb, and Cs) is generated *via* the VESTA software, and the optical properties are analyzed using the complex Kramer's equations.[36] The thermoelectric properties for A_2AlCuF_6 (A = K, Rb, and Cs) are analyzed through the semi-classical approach embedded in the BoltzTraP code. It uses constant relaxation time approximation, which assumes that the charge carrier scattering time (τ) is constant and does not depend on energy or temperature. This simplifies transport calculations by allowing properties like electrical conductivity to be expressed as σ/τ, separating band structure effects from scattering mechanisms.

Results and discussion

Structural attributes

Structural stability ensures that a material maintains its integrity and properties under external conditions, making it reliable for practical applications.[37] The compound A_2AlCuF_6 (A = K, Rb, and Cs) is recognized to exhibit a cubic double perovskite structure with $Fm\bar{3}m$ (225) as the space group. The crystal structures for A_2AlCuF_6 (A = K, Rb, and Cs) are obtained *via* VESTA and are presented in Fig. 1(a and b). In the ball-and-stick representation, the crystal structure clearly highlights the atomic connectivity and individual bond lengths of the A–F, Al–F, and Cu–F bonds. By contrast, in the polyhedral representation, the local coordination environments are emphasized: the AlF_6 and CuF_6 octahedra are depicted as corner-sharing polyhedra, making the octahedral framework and the three-dimensional perovskite network more evident. The A-site of the studied halides (K, Rb, and Cs) occupies coordinates (1/4, 1/4, 3/4), Cu atom placed at the B-site is situated at (1/2, 0, 0), the Al atom situated at the B-site is located at (0, 0, 0), and the F anion is positioned at (0.22, 0, 0). The atomic bond lengths of K–

F, Rb–F, Cs–F, Al–F and Cu–F are noticed as 3.11 Å, 3.37 Å, 3.54 Å, 2.00 Å and 2.46 Å, respectively. The studied structures are then relaxed through a volume optimization technique, which aids in assessing the material's ground state energies. The Birch–Murnaghan equation of state is given as:

$$E(V) = E_0 + \frac{9V_0B_0}{16}\left\{\left[\left(\frac{V}{V_0}\right)^{\frac{2}{3}} - 1\right]^3 B_0' + \left[\left(\frac{V}{V_0}\right)^{\frac{2}{3}} - 1\right]^2\left[6 - 4\left(\frac{V}{V_0}\right)^{\frac{2}{3}}\right]\right\} \quad (3)$$

Fig. 1(c–e) illustrates the optimization plots for K_2AlCuF_6, Rb_2AlCuF_6 and Cs_2AlCuF_6, which revealed a significant increase in the energy and unit cell volume as the A-site is replaced with "K → Rb → Cs". The obtained structural parameters from Birch–Murnaghan equation are listed in Table 1. The obtained lattice parameters for K_2AlCuF_6, Rb_2AlCuF_6 and Cs_2AlCuF_6 revealed a significant increase as the A-site is replaced with K → Rb → Cs. This trend is also justified by the increase in the unit cell volume of the structure obtained *via* volume optimization curves. The obtained bulk modulus reveals a significant decline as the A-site is replaced with K → Rb → Cs, implying stronger bonding and higher lattice rigidity for K_2AlCuF_6. To assess which halide is the most stable among the studied halides, the thermodynamic stability is analyzed, and for this, the formation energies of the studied halides are computed. If the material is energetically favourable with respect to its constituent elements, then its formation energy is obtained as negative; otherwise, the material is concluded to be not energetically favourable and cannot be synthesized. The formation energies for K_2AlCuF_6, Rb_2AlCuF_6 and Cs_2AlCuF_6 are computed as:

Table 1 Optimized lattice parameters for A_2AlCuF_6 (A = K, Rb, and Cs)

Structure parameters	K_2AlCuF_6	Rb_2AlCuF_6	Cs_2AlCuF_6
a (Å)	8.247	8.403	8.633
B (GPa)	69.505	66.083	62.387
B' (GPa)	4.733	4.707	4.780
V_0 (a.u)^3	946.3801	1001.3259	1085.7051
E_0 (Ry)	−7403.962296	−16921.368705	−36156.552417
E_F (eV per atom)	−3.39	−3.35	−3.24
Tolerance factor	0.96	1.00	1.06

$$E_F = E_{Total} - (2E_{K/Rb/Cs} + E_{Al} + E_{Cu} + 6E_F) \quad (4)$$

Here, the individual energies of K/Rb/Cs, Al, Cu and F are represented as $E_{K/Rb/Cs}$, E_{Al}, E_{Cu} and E_F, respectively, while the total energy is denoted as E_{Total}. The obtained formation energies for K_2AlCuF_6, Rb_2AlCuF_6 and Cs_2AlCuF_6 revealed negative values, implying that these halides are energetically favourable with respect to their constituent elements and can be experimentally synthesized. To predict the structural symmetry of these studied perovskite halides, the tolerance factor is computed as:

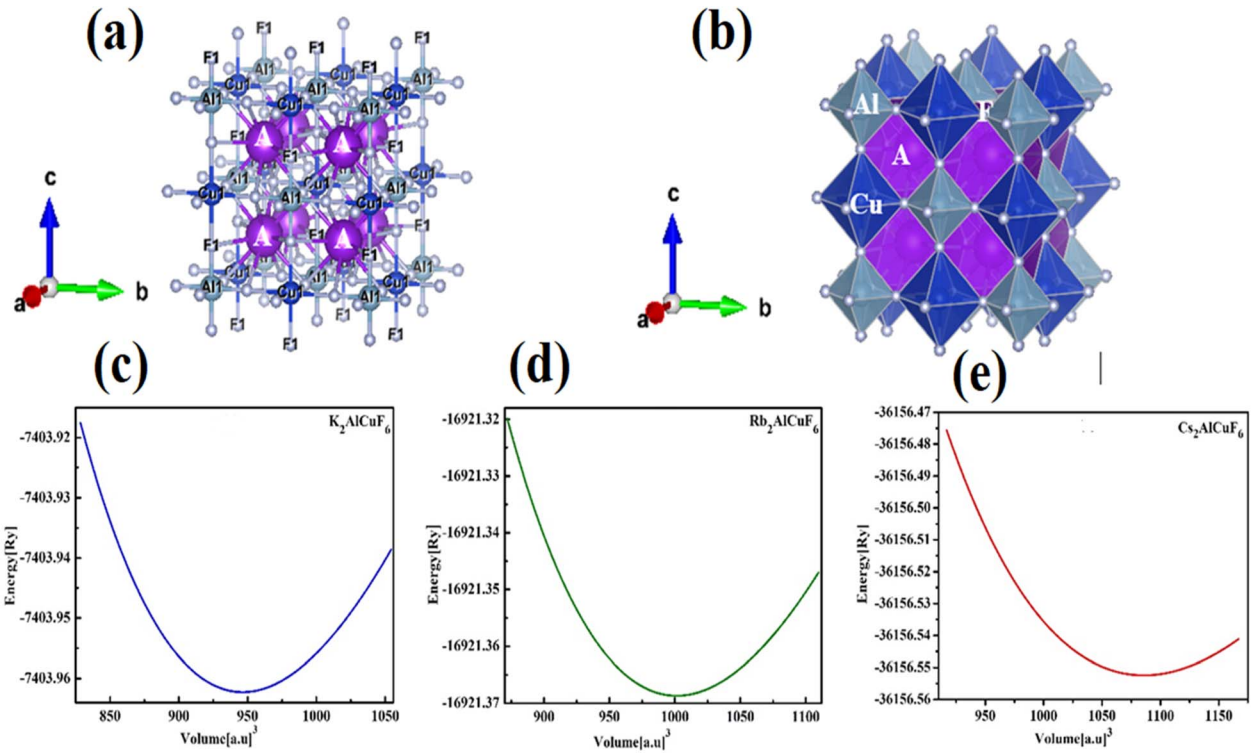

Fig. 1 Crystal structure of A_2AlCuF_6 (A = K, Rb, and Cs) (a) ball to stick model and (b) polyhedral form and (c–e) optimization curves for A_2AlCuF_6 (A = K, Rb, and Cs).

$$\tau = \frac{\left(r_{K/Rb/Cs} + r_F\right)}{\sqrt{2}\left(\frac{r_{Al} + r_{Cu}}{2} + r_F\right)} \quad (5)$$

Here, the Shannon ionic radius is used to assess the tolerance values for the studied halides. The material is predicted to be highly stable when the tolerance value is 1 and exhibit minimal to no distortions, while values below 1 or above 1 imply structural deformities. For cubic perovskite materials with minimal distortion, the tolerance factor should be 0.8 to 1.1.[38] From the obtained tolerance factor values, it is seen that all the studied halides are structurally stable, and this stability increases as the A-site is incorporated with K → Rb → Cs in the studied halides.

Electronic properties

The band structure offers direct insights into the electrical structure and functional behavior of a material. A material's appropriateness for photovoltaic devices, LEDs, photo detectors, and laser devices is determined by the size and kind of bandgap (direct *vs.* indirect).[39] Strong optical absorption and emission are favored by direct bandgap.[40] In this section, we have analyzed the electronic bandgap, TDOS and PDOS of K_2AlCuF_6, Rb_2AlCuF_6 and Cs_2AlCuF_6 with mBJ. Fig. 2 illustrates the electronic properties of K_2AlCuF_6, Rb_2AlCuF_6 and Cs_2AlCuF_6. Indirect bandgaps of 2.80 eV, 2.78 eV and 3.10 eV are noticed for K_2AlCuF_6, Rb_2AlCuF_6 and Cs_2AlCuF_6, respectively, as presented in Fig. 2(a–c), revealing their semiconductor nature. While lattice expansion from K → Rb → Cs reduces orbital overlap and would normally narrow the bandgap, the Cs-based compound deviates due to strong relativistic effects. In Cs, enhanced spin–orbit coupling significantly splits the conduction and/or valence band states, effectively shifting the band edges. Additionally, the larger, more diffused Cs orbitals modify hybridization with neighboring atoms, reducing band dispersion and stabilizing certain states, leading to a reopening (increase) of the bandgap despite the increased lattice constant. The indirect nature of these bandgaps for the studied halides

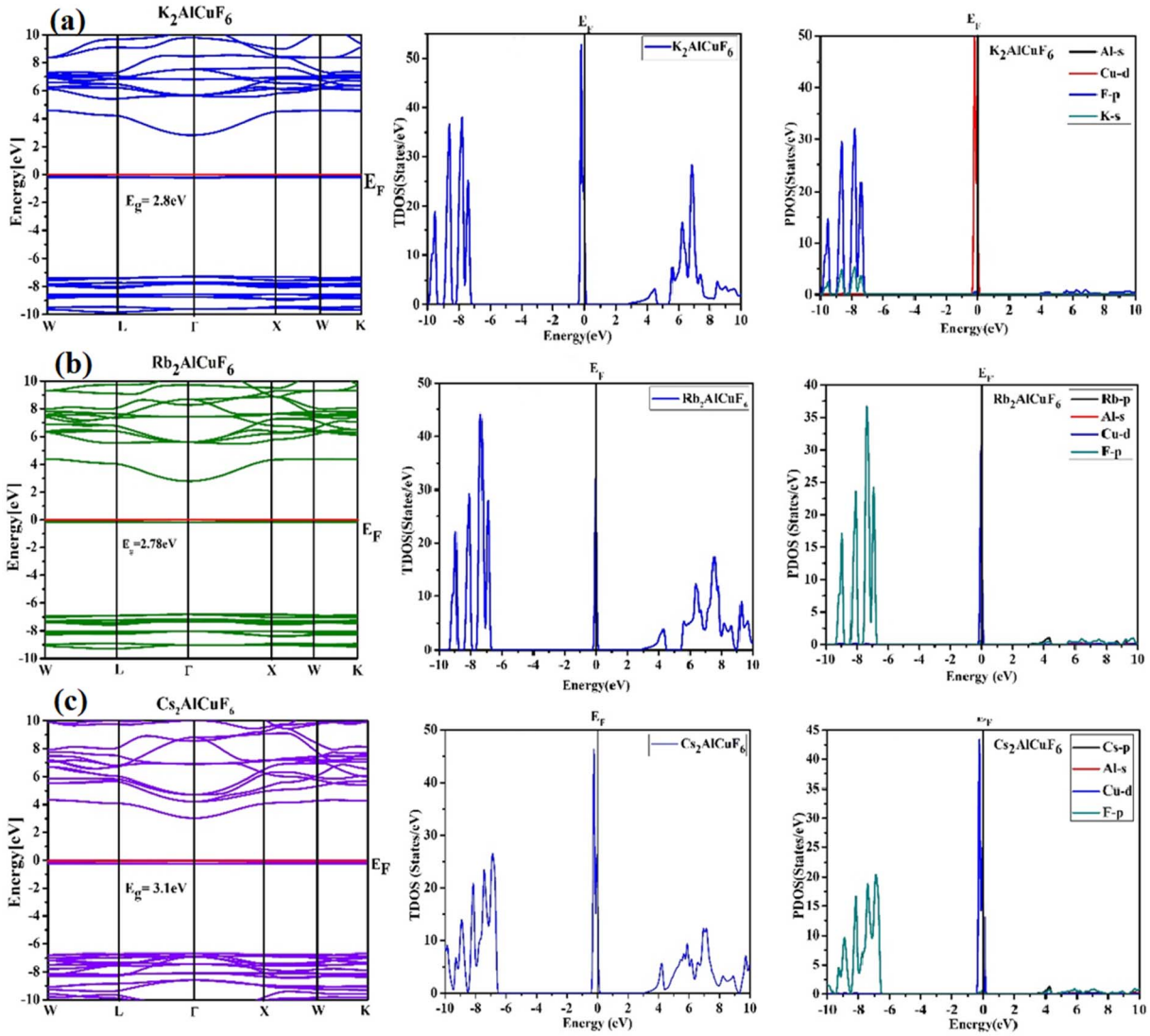

Fig. 2 Electronic properties of (a) K_2AlCuF_6, (b) Rb_2AlCuF_6 and (c) Cs_2AlCuF_6.

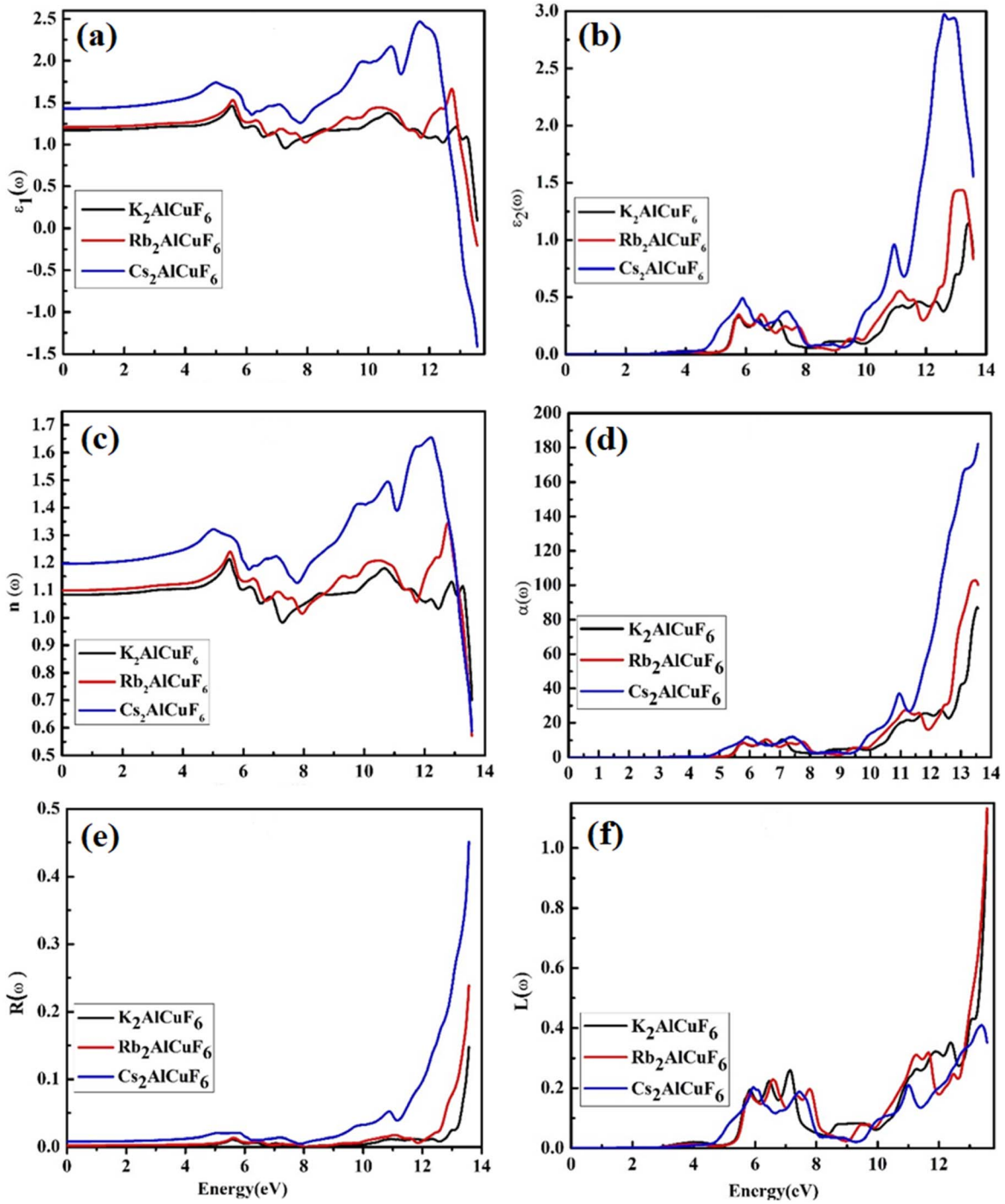

Fig. 3 Optical properties of A_2AlCuF_6 (A = K, Rb, and Cs).

reveals that their efficiency in light-emitting applications is limited as compared to direct-gap materials. Nonetheless, the bandgap values in the near-UV to visible range indicate possible applicability for applications requiring low intrinsic carrier concentration and strong thermal stability as well as for UV optoelectronic devices, dielectric layers, and insulating components. The influence of lattice expansion and electronic structure alteration on the band-edge states is further reflected in the regular fluctuation in bandgap with alkali-metal replacement. Moreover, the TDOS plots, which are plotted parallel to the band structures of K_2AlCuF_6, Rb_2AlCuF_6 and Cs_2AlCuF_6, reveal that the dispersion curves in the electronic band structures perfectly align with the TDOS plots. Significant TDOS features are observed in the valence band region between about −10 eV and 0 eV, but the conduction band states appear above the Fermi level and continue up to around 10 eV. While the broader features in the conduction band suggest more dispersive states, the sharp peaks close to the VBM indicate

Table 2 Computed static values of optical parameters for A_2AlCuF_6 (A = K, Rb, and Cs)

Compound	$\varepsilon(0)$	$n(0)$	$R(0)$
K_2AlCuF_6	1.25	1.08	0.0015
Rb_2AlCuF_6	1.24	1.09	0.0022
Cs_2AlCuF_6	1.40	1.19	0.0079
Similar materials			
K_2SbAuF_6 (ref. 44)	1.93	1.38	0.026
Rb_2SbAuF_6 (ref. 44)	1.96	1.39	0.027
Cs_2InAuF_6 (ref. 45)	1.25	1.11	0.09
Cs_2TlAuF_6 (ref. 45)	2.10	1.49	0.13

relatively concentrated electronic states. Moving from K to Cs causes a systematic widening of the bandgap, which can be explained by lattice expansion and less orbital overlap as the A-site cation radius increases. Furthermore, the PDOS plots for the studied halides are plotted parallel to the TDOS plots, which aid in analyzing the atomic and orbital contributions governing the electronic structure.[41] According to the PDOS plots, the valence band in K_2AlCuF_6 is predominantly dominated by the F-p states, while the Cu-d states report strong hybridization with the F-p states near the top of the valence band, indicating a strong Cu–F covalent interaction. K-s states also exhibit a prominent influence in valence band. For K_2AlCuF_6, the valence band is mainly composed of the Cu-d and F-p states with minor addition from the Al-s and Rb-p states. Similarly, for Cs_2AlCuF_6, the dominance of the Cu-d states near the conduction band is noticed with a slight contribution from the F-p and Cu-s states. The Al-s states report a minor contribution in the valence region for all materials, indicating that aluminum does not actively participate in the formation of the valence band maxima. The contribution of all other states is so small that they are not visible in the graph, so we neglect them. The A-site cations (K, Rb, and Cs) contribute negligibly near the band edges, confirming their ionic role and minimal direct involvement in electronic transport. This behavior indicates that the A-site cations primarily act as charge compensators and structural stabilizers rather than contributing directly to the electronic states responsible for optical and transport properties.

Optical characteristics

The optical analysis of the material describes its interaction with the electromagnetic radiation, which is the fundamental concept in designing the optoelectronic devices.[42] These interactions further lead to multiple phenomena that describe the material's usage in light-harvesting devices.[43] The Kramer–Kronig equations are given below to analyze such phenomena.

$$\varepsilon(\omega) = \varepsilon_1(\omega) + i\varepsilon_2(\omega) \quad (6)$$

Here, the real part is described as $\varepsilon_1(\omega)$, which is associated with the dispersion and polarization in the material caused by the influence of an external electric field, while the imaginary part is represented as $\varepsilon_2(\omega)$ and is associated with the energy loss and absorption of the incident light in the material. The mathematical expression for $\varepsilon_1(\omega)$ and $\varepsilon_2(\omega)$ is given as:

$$\varepsilon_1(\omega) = 1 + \frac{2p}{\pi}\int_0^\infty \frac{\omega'\varepsilon^2\left(\omega'\right)}{\omega'^2 - \omega^2}\mathrm{d}\omega' \quad (7)$$

$$\varepsilon_2(\omega) = \frac{h'e^2}{\pi\omega^2 m^2}\sum_{v\cdot c}\int_{\mathrm{BZ}}^\infty [2M_{cv}(k)]^2\delta[\omega_{cv}(k) - \omega]d^3k \quad (8)$$

The optical properties of K_2AlCuF_6, Rb_2AlCuF_6 and Cs_2AlCuF_6 are presented in Fig. 3. The $\varepsilon_1(\omega)$ of the studied halides is presented in Fig. 3(a). The static $\varepsilon_1(\omega)$ for K_2AlCuF_6, Rb_2AlCuF_6 and Cs_2AlCuF_6 is noticed as 1.25, 1.248 and 1.4, respectively. This increment in the static value is mathematically aligned with the Penn model, which is stated as $\varepsilon_1(\omega) = 1 + \left(\frac{\hbar\omega_p}{E_g}\right)^2$. For all the studied halides, minor peaks are noticed in the energy range of 4 eV to 5 eV, whereas the maximum peaks of $\varepsilon_1(\omega)$ for K_2AlCuF_6, Rb_2AlCuF_6 and Cs_2AlCuF_6 are noticed at 5.56 eV, 12.72 eV and 11.71 eV, respectively. The imaginary part for K_2AlCuF_6, Rb_2AlCuF_6 and Cs_2AlCuF_6 is plotted in Fig. 3(b). Minor peaks are noticed in the range of 5 eV to 8 eV, whereas the maximum peaks are noticed at 13.45 eV, 13.26 eV and 12.62 eV for K_2AlCuF_6, Rb_2AlCuF_6 and Cs_2AlCuF_6, respectively. This trend implies that the studied halides possess high absorption and scattering ability in the UV region. The refractive index $n(\omega)$ defines a material's tendency to bend or slow down light, and for the studied halides (Fig. 3(c)), the static $n(\omega)$ is noticed as 1.08, 1.09 and 1.19 for K_2AlCuF_6, Rb_2AlCuF_6 and Cs_2AlCuF_6, respectively, which gradually increases to the maximum values of $n(\omega)$, reported at 5.56 eV, 12.80 eV and 12.20 eV, respectively. This implies that at low energies, the materials are very transparent. For the studied halides, the refractive index rises as photon energy increases because light interacts more intensely. Strong electronic transitions, which show the energies where the optical dispersion is the greatest, are correlated with the peak refractive index. The absorption coefficient describes a material's strength to absorb the incident light per unit centimeter, and for the studied halides, it is plotted in Fig. 3(d). Minor peaks of absorption coefficient are reported from 5 eV to 8 eV, whereas the maximum absorption peaks are noticed at 13.56 eV for K_2AlCuF_6, Rb_2AlCuF_6 and Cs_2AlCuF_6. Among the studied halides, Cs_2AlCuF_6 reports the maximum value of absorption coefficient, which implies this material is highly suitable for protection against UV radiation as compared to K_2AlCuF_6 and Rb_2AlCuF_6. The reflectivity of a material describes its ability to reflect the incident light, and Fig. 3(e) demonstrates the reflectivity plots for K_2AlCuF_6, Rb_2AlCuF_6 and Cs_2AlCuF_6. The reflectivity for K_2AlCuF_6, Rb_2AlCuF_6 and Cs_2AlCuF_6 is noticed at 0.0015, 0.0022 and 0.0079, while the maximum reflectivity peaks are noticed at 13.56 eV in the UV region. The energy loss function defines the dissipation and scattering phenomena in a material, and for K_2AlCuF_6, Rb_2AlCuF_6 and Cs_2AlCuF_6, it is plotted in Fig. 3(f). The energy loss function plot suggests that the minimum energy loss peaks for the studied halides are

noticed in the energy range of 5 eV to 8 eV, whereas the maximum peaks are noted at 13.45 eV, 13.26 eV and 12.62 eV for K_2AlCuF_6, Rb_2AlCuF_6 and Cs_2AlCuF_6, respectively. According to the optical study, K_2AlCuF_6, Rb_2AlCuF_6 and Cs_2AlCuF_6 have low static refractive indices and are extremely transparent at low photon energies. Refractive index, absorption, and reflectivity increase with photon energy, suggesting increased light-matter interactions and electronic transitions. The UV area has the highest absorption and energy loss peaks, indicating that these halides have a high capacity for scattering and dissipation. Cs_2AlCuF_6 has the maximum absorption among all the studied halides, which makes it ideal for light-harvesting and UV protection applications. The computed optical parameters for A_2AlCuF_6 (A = K, Rb, and Cs) are comparable with similar perovskite fluorides, as presented in Table 2.

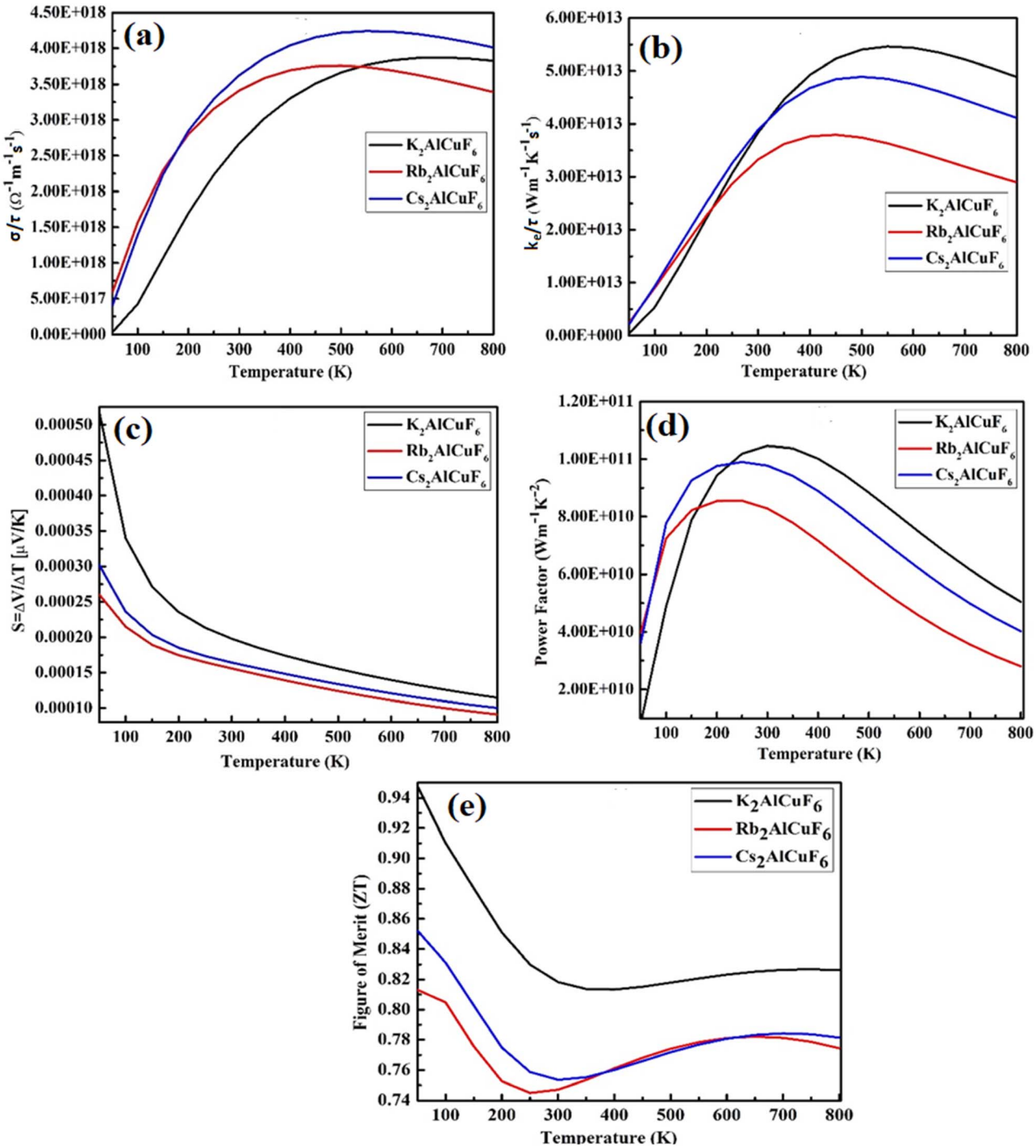

Fig. 4 Thermoelectric properties of A_2AlCuF_6 (A = K, Rb, and Cs).

Thermoelectric properties

In order to address the global energy issues and reduce environmental pollution, new energy materials are essential.[46] Thermoelectric materials are environmentally friendly functional materials that can directly transform heat energy into electrical energy. Because of their many useful applications, such as in radioisotope thermoelectric generators, and benefits such as waste heat utilization, thermoelectric materials are regarded as promising candidates for addressing the challenges of energy crises.[47] Scientists are in constant search for materials that can convert waste heat into useful energy. In this context, perovskite halides are considered an exceptional choice for the production of green energy as these materials possess favorable thermoelectric properties, including lower thermal conductivity and higher electrical conductivity.[48–50] In this section, we investigated the thermoelectric potential of K_2AlCuF_6, Rb_2AlCuF_6 and Cs_2AlCuF_6 by employing the semi-classical approach implemented in the BoltzTraP code. The thermoelectric properties computed for K_2AlCuF_6, Rb_2AlCuF_6 and Cs_2AlCuF_6 are presented in Fig. 4. Fig. 4(a) demonstrates the electrical conductivity plots for K_2AlCuF_6, Rb_2AlCuF_6 and Cs_2AlCuF_6. In a semiconducting material, the electrical conductivity is described as $\sigma = ne\mu + np\mu$. Here "$ne\mu$" represents the conductivity in the conduction band due to electrons, whereas "$np\mu$" represents the conductivity in the valence band due to holes. The electrical conductivity is noticed as zero for K_2AlCuF_6 at 50 K, whereas for Rb_2AlCuF_6 and Cs_2AlCuF_6, the electrical conductivity is noticed as $6.0 \times 10^{17}\ \Omega^{-1}\ m^{-1}\ s^{-1}$ and $4.0 \times 10^{17}\ \Omega^{-1}\ m^{-1}\ s^{-1}$, respectively. With the increase in temperature, the σ/τ increases for all the three studied halides, and maximum peaks of electrical conductivities for K_2AlCuF_6 and Rb_2AlCuF_6 are noticed at 500 K as $3.75 \times 10^{18}\ \Omega^{-1}\ m^{-1}\ s^{-1}$, whereas for Cs_2AlCuF_6, the maximum electrical conductivity is observed as $4.25 \times 10^{18}\ \Omega^{-1}\ m^{-1}\ s^{-1}$. Moreover, it is noticed that as the temperature is increased, the conductivities of all the halides decline. Fig. 4(b) demonstrates the thermal conductivity plots for K_2AlCuF_6, Rb_2AlCuF_6 and Cs_2AlCuF_6. The capacity of a material to conduct heat is known as thermal conductivity. It measures the effectiveness of thermal energy transfer through a material, either by electrons in metals or lattice vibrations in insulators.[51] While low-conductivity materials function as thermal insulators, high-conductivity materials transport heat rapidly. As we are employing BoltzTraP, it only aids in assessing the electronic thermal conductivity. The thermal conductivity plots for K_2AlCuF_6, Rb_2AlCuF_6 and Cs_2AlCuF_6 reveal an increasing trend with temperature, and the maximum values are noticed at 400 K, 500 K and 550 K as $5.5 \times 10^{13}\ Wm^{-1}\ K^{-1}\ s^{-1}$, $3.8 \times 10^{13}\ Wm^{-1}\ K^{-1}\ s^{-1}$ and $4.8 \times 10^{13}\ Wm^{-1}\ K^{-1}\ s^{-1}$ for K_2AlCuF_6, Cs_2AlCuF_6 and Rb_2AlCuF_6, respectively. Furthermore, it is noticed that the thermal conductivities for all the studied halides decline as temperature is increased. Among the studied halides, K_2AlCuF_6 has the highest thermal conductivity, indicating the most efficient heat transfer mechanism and better heat dissipation in thermal devices based on it than in devices based on Cs_2AlCuF_6 and Rb_2AlCuF_6. The Seebeck coefficient aids in analyzing a material's tendency to generate thermal voltage under the influence of a temperature gradient.[52] A tiny variation in the material's temperature gradient leads to higher thermal voltage generation, resulting in a higher Seebeck coefficient, which is crucial for effective thermoelectric devices. The Seebeck coefficient of K_2AlCuF_6, Rb_2AlCuF_6 and Cs_2AlCuF_6 is demonstrated in Fig. 4(c). At 50 K, the Seebeck coefficient values for K_2AlCuF_6, Rb_2AlCuF_6 and Cs_2AlCuF_6 are noticed to be 530 $\mu V\ K^{-1}$, 300 $\mu V\ K^{-1}$ and 256 $\mu V\ K^{-1}$, respectively. These values suggest that all the three halides are excellent contenders for generating thermal voltage at lower temperatures; however, as the temperature is raised, the Seebeck coefficient declines to 120 $\mu V\ K^{-1}$, 110 $\mu V\ K^{-1}$ and 100 $\mu V\ K^{-1}$ at 800 K for K_2AlCuF_6, Rb_2AlCuF_6 and Cs_2AlCuF_6, respectively. A material's ability to convert waste heat into useful energy is demonstrated through its power factor, which is plotted in Fig. 4(d) for K_2AlCuF_6, Rb_2AlCuF_6 and Cs_2AlCuF_6. A higher value of power factor indicates a better thermoelectric energy conversion efficiency. Initially at 50 K, the value of power factor for K_2AlCuF_6, Rb_2AlCuF_6 and Cs_2AlCuF_6 is reported to be $1.0 \times 10^{10}\ Wm^{-1}\ K^{-2}$, $4.0 \times 10^{10}\ Wm^{-1}\ K^{-2}$ and $3.8 \times 10^{10}\ Wm^{-1}\ K^{-2}$, respectively. At 300 K, 200 K and 250 K, the maximum values of the power factor is reported for K_2AlCuF_6, Rb_2AlCuF_6 and Cs_2AlCuF_6 as $1.04 \times 10^{11}\ Wm^{-1}\ K^{-2}$, $8.1 \times 10^{10}\ Wm^{-1}\ K^{-2}$ and $1.0 \times 10^{11}\ Wm^{-1}\ K^{-2}$, respectively. This suggests that among the studied halides, K_2AlCuF_6 possesses the highest thermoelectric efficiency. The figure of merit is a dimensionless quantity, which is the most crucial thermoelectric trait in analyzing the thermoelectric properties of any material. Materials with high ZT values are considered viable for exhibiting good thermoelectric performance.[53] Fig. 4(e) depicts the ZT plots of K_2AlCuF_6, Rb_2AlCuF_6 and Cs_2AlCuF_6. At 50 K, the ZT values for K_2AlCuF_6, Rb_2AlCuF_6 and Cs_2AlCuF_6 are noticed as 0.95, 0.81 and 0.85, respectively, which implies that at lower temperatures, the studied halides possess a higher Seebeck coefficient value, which is directly linked with the materials ZT value. Furthermore, as the temperature is increased till 250 K-300 K, the ZT value declines to 0.82, 0.74 and 0.76 for K_2AlCuF_6, Rb_2AlCuF_6 and Cs_2AlCuF_6, respectively. These thermoelectric traits for the studied halides reveal that K_2AlCuF_6 is an exceptional contender for the production of green energy compared to Rb_2AlCuF_6 and Cs_2AlCuF_6.

The computed thermoelectric parameters for A_2AlCuF_6 (A = K, Rb, and Cs) are comparable with similar perovskite fluorides, as presented in Table 3.

Table 3 Computed thermoelectric parameters for A_2AlCuF_6 (A = K, Rb, and Cs)

Compounds	σ/τ	k_e/τ	ZT
K_2AlCuF_6	3.75×10^{18}	5.5×10^{13}	0.82
Rb_2AlCuF_6	3.75×10^{18}	3.8×10^{13}	0.74
Cs_2AlCuF_6	4.25×10^{18}	4.8×10^{13}	0.76
Similar materials			
K_2SbAuF_6 (ref. 44)	1.99×10^{18}	4.9×10^{13}	0.76
Rb_2SbAuF_6 (ref. 44)	2.28×10^{18}	5.4×10^{13}	0.75

Conclusion

In conclusion, double perovskites A_2AlCuF_6 (A = K, Rb, and Cs) exhibit promising properties for renewable energy harvesting, as revealed by the first-principles DFT-based simulation. Structural analysis shows that replacing the A-site cation from K → Rb → Cs leads to an increase in lattice constants, unit cell volumes, and ground-state energies, accompanied by a decreasing bulk modulus. Negative formation energies and favorable tolerance factors confirm the thermodynamic and structural stability of these compounds. Electronic structure calculations indicate indirect bandgap that increase along the series (2.80 eV for K_2AlCuF_6, 2.78 eV for Rb_2AlCuF_6, and 3.10 eV for Cs_2AlCuF_6), while optical analysis identifies Cs_2AlCuF_6 as the most efficient UV absorber with minimal energy loss, making it a strong candidate for UV shielding and photodetector applications. Furthermore, thermoelectric properties computed *via* BoltzTraP reveal high *ZT* values at elevated temperatures, highlighting the potential of all the three halides for waste-heat energy conversion. Overall, these findings position A_2AlCuF_6 (A = K, Rb, and Cs) perovskites as versatile materials for optoelectronic and thermoelectric energy applications.

Conflicts of interest

The authors have declared no conflicts of interest.

Data availability

All data produced are available in the manuscript. The authors have no extra data to declare.

Acknowledgements

The authors express their gratitude to Princess Nourah bint Abdulrahman University Researchers Supporting Project number (PNURSP2026R943), Princess Nourah bint Abdulrahman University, Riyadh, Saudi Arabia.

References

1 S. M. Mahi, L. R. Paul and M. A. Rashid, Mechanical, optoelectronic and thermoelectric response of oxide double perovskites Ca_2VXO_6 (X= In, Tl) for sustainable energy application, *Mater. Today Commun.*, 2026, 114620.
2 K. El Kihel, *et al.*, Electronic structure, Optical, Phonon, Mechanical, Thermodynamic, and Hydrogen Storage properties of A2BH6 (A= Ca, Sr, Ba) perovskite hydrides by DFT calculations, *Phys. B*, 2026, 418219.
3 J. Munir, *et al.*, First-principles investigations of the mechanically and thermodynamically stable potassium-based double perovskites K2TlAsX6 (X= Cl, Br) for optoelectronic and renewable applications, *Mater. Sci. Eng., B*, 2023, **298**, 116830.
4 M. Hou, *et al.*, NiX (X= Co, Cr, Cu, Fe, Ni, Mn, Ti, V) co-doped N6-graphene as efficient trifunctional electrocatalyst for the HER, OER and ORR: A density functional theory study, *Int. J. Hydrogen Energy*, 2026, **202**, 153029.
5 W. Fan, Z. Sun and R. J. N. Xiao, A novel method to rapidly functionalize perovskite oxide, *Nanoscale*, 2026, 3387–3398.
6 H. Murtaza, *et al.*, Influence of B′-site vacancy on hydrogen storage, structural, elastic, thermodynamic and optoelectronic attributes of potassium based double perovskite K2LiAlH6hydride for green energy applications, *Sci. Rep.*, 2025, in press.
7 A. Javed, *et al.*, Spin-Polarized DFT Based Investigation of Cs2LiMoBr6: A Promising Candidate for Spintronics, Optoelectronics and Sustainable Energy Systems, *J. Supercond. Novel Magn.*, 2026, **39**(1), 30.
8 T. Liu, *et al.*, Inter-facial chemical Ti-O-Cd bond to facilitate the charge transfer of in-situ growth 0D/1D CdS-TiO2 nanostructure toward highly-efficient solar to hydrogen conversion, *J. Alloys Compd.*, 2026, 187391.
9 S. M. Qaid, *et al.*, First-principles investigations on the structural, optoelectronic, mechanical and transport properties of new stable lead-free double perovskites Cs2BB' I6 (B= Ag/Rb, B′= Bi/Ga) halides, *Mater. Sci. Eng., B*, 2024, **301**, 117176.
10 J. Munir, *et al.*, Electronic structure, optical and thermal response of lead-free RbAuBr3 and RbAuBr4 perovskites for renewable energy applications, *ECS J. Solid State Sci. Technol.*, 2022, **11**(12), 123003.
11 Y. Yang, *et al.*, Origin of the stability of two-dimensional perovskites: a first-principles study, *J. Mater. Chem. A*, 2018, **6**(30), 14949–14955.
12 A. M. Ganose, C. N. Savory and D. O. Scanlon, Beyond methylammonium lead iodide: prospects for the emergent field of ns 2 containing solar absorbers, *Chem. Commun.*, 2017, **53**(1), 20–44.
13 P. P. Boix, *et al.*, Perovskite solar cells: beyond methylammonium lead iodide, *J. Phys. Chem. Lett.*, 2015, **6**(5), 898–907.
14 P. Saikia, *Study of the Sensing and Photocatalytic Potentials of Some Perovskite-Based Materials*, Tezpur University, 2023.
15 H. Murtaza, *et al.*, The effect of pressure in tuning the optoelectronic, thermoelectric and hydrogen storage properties of RbCaH3 for renewable energy applications, *J. Energy Storage*, 2025, **134**, 118183.
16 J. Munir, *et al.*, Electronic structure and optical and thermoelectric response of lead-free double perovskite BaMgLaBiO6: a first-principles study, *J. Comput. Electron.*, 2023, **22**(5), 1482–1494.
17 I. Mursaleen, *et al.*, The influence of bandgap tunability on the physical features of Rb2LiSbX6 (X= Cl, Br) double perovskites in the context of green technologies, *Phys. B*, 2025, **697**, 416695.
18 M. Leblanc, V. Maisonneuve and A. Tressaud, Crystal chemistry and selected physical properties of inorganic fluorides and oxide-fluorides, *Chem. Rev.*, 2015, **115**(2), 1191–1254.
19 H. Qiu, S. Pan and M. Mutailipu, Fluorination strategy toward chemical and functional modification, *Fundam. Res.*, 2025, **5**(2), 640–653.

20 Z. Chen, *et al.*, Conformational Editing Drives Covalent Hybridization for Nonlinear Optical Crystals, *Angew. Chem., Int. Ed.*, 2026, e8834948.
21 X. Long, *et al.*, Integrating Fluorinated [BF4] Anion With π-Conjugated Six-Membered Rings for Short-Wavelength UV Frequency Conversion, *Angew. Chem., Int. Ed.*, 2026, **65**(3), e22210.
22 B. Ai, Z. Fan and Z. J. Wong, Plasmonic–perovskite solar cells, light emitters, and sensors, *Microsyst. Nanoeng.*, 2022, **8**(1), 5.
23 A. A. Ugochukwu, *et al.*, Recent enhancement in photovoltaic cell efficiency performance, stability, and cost reduction: a review, *Sol. Energy*, 2025, **300**, 113853.
24 J. Munir, *et al.*, First-principles scrutiny of double perovskite halides A2AlAuCl6 (A= Cs, K, Rb): potential contenders for renewable energy, *Arabian J. Sci. Eng.*, 2025, **50**(9), 6511–6522.
25 H. Qian, *et al.*, A comprehensive DFT of structural, electrical, elastic, and optical properties of CsGeF3 perovskite under hydrostatic pressure, *Mater. Sci. Eng., B*, 2026, **323**, 118819.
26 F. S. Rodrigues, *et al.*, Theoretical Design and Characterization of Rb2ZnRuCl6 and Cs2ZnRuCl6 Novel Halide Perovskites, *ChemNanoMat*, 2026, **12**(1), e202500645.
27 M. J. Islam and R. Amin, DFT-based numerical study of Cs3QR6 (Q= In, Tl, Ga; R= I, Cl, Br) compounds for opto-solar applications, *Mater. Res. Express*, 2026, **13**(1), 015902.
28 A. Laassouli, *et al.*, Novel Insights into the Electric Field-Driven Electronic and Optical Behavior of K2AgSbI6 *via* DFT, *J. Electron. Mater.*, 2026, 1–13.
29 M. R. Islam, First-principles analysis of eco-friendly Sr 3 BiX 3 (X= I, Br, and Cl) inorganic perovskites for optoelectronic applications: a DFT–ML hybrid approach, *New J. Chem.*, 2026, **50**(1), 522–536.
30 A. N. Khan, *et al.*, Multi-functional DFT and SCAPS-1D analysis of lead-free Z2MgGeI6 (Z= Na, K) double perovskites for optoelectronic, photo-catalytic, and photovoltaic applications, *Sol. Energy Mater. Sol. Cells*, 2026, **294**, 113922.
31 N. Naeem, *et al.*, Structural, Mechanical, Optoelectronic, and Transport Characteristics of Eco-Friendly Double Perovskites Li2ScAuZ6 (Z= Cl or Br or I) For Energy Harvesting: A Density Functional Theory Approach, *Braz. J. Phys.*, 2026, **56**(1), 1–18.
32 T. Al Galib, *et al.*, Ab initio study of lead-free K_2ScInX_6 (X= F, Cl, Br, I) halide double perovskites for sustainable optoelectronics, *Comput. Theor. Chem.*, 2026, 115681.
33 D. Islam, *et al.*, Novel A2MgZnX6 halide double perovskites: Stable and non-toxic materials for solar energy harvesting, *Mod. Phys. Lett. B*, 2026, 2650038.
34 K. Choudhary and F. Tavazza, Convergence and machine learning predictions of Monkhorst-Pack k-points and plane-wave cut-off in high-throughput DFT calculations, *Comput. Mater. Sci.*, 2019, **161**, 300–308.
35 P. Ziesche, S. Kurth and J. P. Perdew, Density functionals from LDA to GGA, *Comput. Mater. Sci.*, 1998, **11**(2), 122–127.
36 Z. Ur Rehman, *et al.*, First principles study of Rb2NaGaX6 (X= Br, Cl) double perovskites: Structural, mechanical, vibrational, electronic, optical, SLME, thermoelectric and thermodynamic properties for solar cell applications, *J. Phys. Chem. Solids*, 2025, **199**, 112489.
37 Y. Wang, *et al.*, Enhanced structural stability of P2-type Mn/Fe-based layered oxide by high entropy doping towards long-life sodium ion battery cathode, *Appl. Surf. Sci.*, 2025, **693**, 162799.
38 R. N. Mondal, *et al.*, Unveiling Thermal, Phonon, and Optoelectronic Characteristics of Cs3OX (X= Cl, Br, or I) Antiperovskites for Sustainable Energy Applications: A DFT Exploration, *Int. J. Energy Res.*, 2026, **2026**(1), 5561106.
39 A. S. Jbara, *et al.*, Investigation of the Lead-Free Perovskites AlSnX3 (X= Cl, Br, I) for Optoelectronic Applications: A First-Principles Analysis, *J. Inorg. Organomet. Polym. Mater.*, 2025, 1–12.
40 E. Carvajal, *et al.*, Electronic properties of double perovskite compounds, *Phys. Status Solidi B*, 2005, **242**(9), 1942–1945.
41 J. Munir, *et al.*, Electronic structure and optical properties of lead-free double perovskite BaMgLaBiO6: a DFT study. in *Proceedings of the 7th International Conference on the Applications of Science and Mathematics 2021: Sciemathic 2021*, Springer, 2022.
42 Y. Hao, *et al.*, Characteristics of carrier localization and their effects on minority carrier lifetime in InAs/In0. 5Ga0. 5As0. 5Sb0. 5 type II superlattices, *Appl. Phys. Lett.*, 2025, **127**(8), 082105.
43 S. M. Qaid, *et al.*, Exploring spin-polarized structural, ferromagnetic, optoelectronic, thermodynamic, and mechanical attributes of lead-free Cs2GdAuX6 (X= Br/I) double perovskites for spintronics and green energy applications, *Opt. Mater. Express*, 2025, **16**(1), 141–154.
44 I. Ahmad, *et al.*, Exploring the semiconductor character of Z2SbAuF6 (Z= K, Rb) halide double perovskites for the latest technology applications, *Mater. Chem. Phys.*, 2026, 132413.
45 M. Jamil, *et al.*, A first-principles investigation on the structural, optoelectronic, mechanical and thermoelectric properties of double Cs2XAuF6 (X= Al, Ga) perovskites for green energies: M Jamil et al, *Indian J. Phys.*, 2025, 1–12.
46 I. U. Islam, *et al.*, PASP-coated bimetallic mustard husk hydrochar for dual environmental remediation and green energy: Pb (II) removal, enhanced hydrogen evolution, and DFT insights aligned with UN SDGs, *Fuel*, 2026, **410**, 137930.
47 D. Chu, *et al.*, Unbiased Screening of Novel Infrared Nonlinear Optical Materials with High Thermal Conductivity: Long-neglected Nitrides and Popular Chalcogenides, *Angew. Chem.*, 2023, **135**(16), e202300581.
48 H. Murtaza, *et al.*, An in-depth analysis of the optoelectronics, phonon, mechanical, thermodynamic and transport attributes of lead-free K2TlInX6 (X= I, Br) double perovskites for green energies, *Int. J. Mod. Phys. B*, 2026, 2650044.
49 I. Mursaleen, *et al.*, The spin-polarized computations on the mechanical, structural, electronic, magnetic, transport and optical traits of A2BMoI6 (A= K/Rb; B= Rb/Li) double

perovskites for sustainable energy applications, *Mod. Phys. Lett. B*, 2026, **40**(06), 2650018.

50 N. Ahmed, *et al.*, A comprehensive insight to the mechanical, thermodynamic, structural, transport and optoelectronic attributes of (B/Al/Ga) SbO3 for sustainable energy applications, *J. Electroceram.*, 2025, 1–14.

51 A. N. Rathod and A. M. Vora, First-principles investigation of the elastic, thermodynamic, and thermoelectric properties of NaAlSn, *Mod. Phys. Lett. B*, 2026, 2650035.

52 K. R. Panday, *et al.*, Unveiling the Thermoelectric Properties of Some Bismuth Based Half Heuslers: A First-Principles Perspective, *Adv. Theory Simul.*, 2026, **9**(1), e01816.

53 G. Mahan, Figure of merit for thermoelectrics, *J. Appl. Phys.*, 1989, **65**(4), 1578–1583.